Microfluidics and Nanofluidics

Microfluidic device with dual-channel fluorescence acquisition for quantfication/identification of cancer cells

--Manuscript Draft--

Manuscript Number:	MANO-D-17-00097
Full Title:	Microfluidic device with dual-channel fluorescence acquisition for quantfication/identification of cancer cells
Article Type:	Original Article
Corresponding Author:	Eric Pedrol, MSc Universitat Rovira i Virgili Tarragona, Tarragona SPAIN
Corresponding Author Secondary Information:	
Corresponding Author's Institution:	Universitat Rovira i Virgili
Corresponding Author's Secondary Institution:	
First Author:	Eric Pedrol
First Author Secondary Information:	
Order of Authors:	Eric Pedrol
	Javier Martínez
	Magdalena Aguiló
	Manuel Garcia-Algar
	Moritz Nazarenus
	Luca Guerini
	Eduardo Garcia-Rico
	Ramón Álvarez-Puebla
	Francesc Díaz
	Jaume Massons
Order of Authors Secondary Information:	
Funding Information:	Ministerio de Economía y Competitividad (mat2013-47395-C4-4-R) — Not applicable
	Ministerio de Economía y Competitividad (TEC2014-55948-R) — Not applicable
	Ministerio de Economía y Competitividad (CTQ2014-59808R) — Not applicable
	Generalitat de Catalunya (2014SGR1358) — Not applicable
	Generalitat de Catalunya (2014SGR480) — Not applicable
	AEI/FEDER EU (MAT2016- 75716-C2-1-R) — Not applicable
Abstract:	An optofluidic device for cell discrimination with two independent interrogation regions is presented. Pumping light coupling to the device and cells' fluorescence extraction from the two interrogation zones is accomplished employing optical fibers embedded in said optofluidic chip. To test the reliability of this device AU-565 cells -expressing EpCAM and HER2

	receptors- and RAMOS cells were mixed in a controlled manner, confined inside an hydrodynamic focused flow in the microfluidic chip and detected individually to be later discriminated as positive (signal re- ception from fluorescently labeled antibodies from the AU-565 cells) or negative events (RAMOS cells). A correlation analysis is performed over the two intensity versus time signals obtained at each of the two interrogation zones. A post-processing analysis permits a peak-to-peak pairing between the two output signals, being the detected peaks at each channel events related to the passing of a single cell through an interrogation region. Said method reduces the influence of noise on the overall data and allows to better discern actual cells' characteristic intensity bursts from noise without the need of digitally aided signal processing.
Suggested Reviewers:	Tayfun Akin, Dr in Electrical and Electronics Engineering Prof. Dr., Director, METU-MEMS Center tayfuna@metu.edu.tr
	Piotr Garstecki, DSc in Physical Chemistry Professor, Insititute on Physical Chemistry of Polish Academy of Sciences, Warsaw, Poland garst@ichf.edu.pl
	Wolfgang Parak Professor, Philipps-Universitat Marburg wolfgang.parak@physik.uni-marburg.de
	Xing Yi Ling, PhD in Chemistry Assistant Chair (Faculty), School of Physical & Mathematical Sciences Associate, Nanyang Technological University xyling@ntu.edu.sg Expert in spectroscopy
	Laura Fabris, PhD in in Chemical Sciences Associate Professor, Rutgers The State University of New Jersey lfabris@rci.rutgers.edu Expert in cell detection with spectroscopy
	Juan Casado Professor of Physical Chemistry and Spectroscopy, Universidad de Malaga casado@uma.es Expert in fluorescence
	Mona Tréguer-Delapierre, PhD in chemistry Assistant Professor, Institut de Chimie de la Matiere Condensee de Bordeaux mona.treguer-delapierre@icmcb.cnrs.fr Expert in microfluidics
	Alex Wei alexwei@purdue.edu

Noname manuscript No.
(will be inserted by the editor)

Microfluidic device with dual-channel fluorescence acquisition for quantification/identification of cancer cells

Eric Pedrol · Javier Martínez · Magdalena Aguiló · Manuel Garcia-Algar · Moritz Nazarenus · Luca Guerrini · Eduardo Garcia-Rico · Ramón A. Álvarez-Puebla · Francesc Díaz · Jaume Massons

Data

Abstract An optofluidic device for cell discrimination with two independent interrogation regions is presented. Pumping light coupling to the device and cells' fluorescence extraction from the two interrogation zones is accomplished employing optical fibers embedded in said optofluidic chip. To test the reliability of this device AU-565 cells -expressing EpCAM and HER2 receptors- and RAMOS cells were mixed in a controlled manner, confined inside an hydrodynamic focused flow in the microfluidic chip and detected individually to be later discriminated as positive (signal re- ception from fluorescently labeled antibodies from the AU-565 cells) or negative events (RAMOS cells). A correlation analysis is performed over the two intensity versus time signals obtained at each of the two interrogation zones. A post-processing analysis permits a peak-to-peak pairing between the two output signals, being the detected peaks at each channel events related to the passing of a single cell through an interrogation region. Said method reduces the influence of noise on the overall data and allows to better discern actual cells' characteristic intensity bursts from noise without the need of digitally aided signal processing.

Eric Pedrol
Física i Cristal·lografia de Materials i Nanomaterials (FiCMA-FiCNA) and EMaS, Universitat Rovira i Virgili (URV), Campus Sescelades, Marcel·lí Domingo, 1, E-43007, Spain
E-mail: eric.pedrol@urv.cat

1 Introduction

Microfluidic devices have emerged as a tool for low cost solutions for analytical challenges for environmental, industrial and medical diagnosis. Poly(dimethylsiloxane) has been one of the most intensively used polymers for microfluidics, because its chemical and physical properties make possible fabrication of devices with useful functionalities (McDonald and Whitesides 2002). The minimal reagent requirements, its low cost of production and automation make them an invaluable component for current innovations in point-of-care diagnostics (Gervais et al. 2011).

Optofluidic devices can make use of light-scattering (Schafer et al. 2009; Konokhova et al. 2012; Weigl et al. 2001), surface-enhanced Raman scattering (Català et al. 2016; Pazos-Pérez et al. 2016; Pelaz et al. 2017), light-blocking (Schaap et al. 2012) or fluorescence-based methods. In general, fluorescence related techniques encompass higher sensitivity for particle detection (Chen and Wang 2009). Non-fluorescent samples require functionalization with fluorescent species (i.e., fluorophores or fluorescent particles). In the case of cells, these fluorescent species can be coupled to molecules capable of recognizing specifically determined membrane receptors allowing for the high-throughput screaning of complex samples (Bouzigues et al. 2011; Wang et al. 2009). This has applications to the diagnosis of diseases.

For cell discrimination, it is necessary to discern individual cells flowing inside a microfluidic channel. Different solutions have been proposed to avoid undesired simultaneous multiple detections. One of them is to limit the capture of light from the interrogation zone to a confocal volume; confocal microscopes are optical arrangements commonly used for particle dynamic flow parameters determination and light signal analysis (Edel and Mello 2003). A different approach for single-cell detection relies on the use of narrow pumping areas. Instead of optically limiting light collection from a relatively big pumping volume, as in confocal microscopy, an equally valid solution is to restrict, by optical means, the illuminated volume; the interrogation zone becomes the illuminated region itself. For that purpose, many authors suggest the use of embedded optical fibers and waveguides in microfluidic chips to either pump fluorescent particles flowing in a microfluidic channel or to collect its fluorescence or both (Chang-Yen et al. 2005; Garcia et al. 2012). Hydrodynamic focusing of the sample flow allows, working in conjunction with this later method, for an additional refinement to limit even more the interrogation zone (Knight et al. 1998; Tung et al. 2004). The simplest description of a microfluidic chip with hydrodynamic focusing capabilities is a cross-shaped channel structure. The fluid containing the sample is injected in one of the channels whereas a sacrificial fluid, or sheath flow, is injected at the same time through the two adjacent channels spatially limiting the width of the developed central laminar sample flow at the t-junction. Due to the involved low time scales and the magnitude of the diffusion rate in a typical experiment, both sheath and sample flows seem to be not mixing at all as the focused sample flow and the adjacent sheath flows are being driven toghether across the remaining microfluidic channel. Hydrodynamic spatial confinement can be extended to the vertical direction to further restrict the sample flow development in what's known as 3D hydrodynamic focusing (Chang et al. 2007; Jiang et al 2013; Daniele et al. 2015; Lu et al. 2016). In this case the flow is focused in an additional direction perpendicular to the flow's moving direction behaving as a linear stream of flow confined in two directions. Aiming at substantially improve the detection efficiency in fluorescent particles measurements, many autors have proposed to join, in a single optofluidic device, 3D focusing capabilities and the portability of optical fibers (Mao et al. 2012; Testa et al. 2015).

In our work, we describe a 3D flow focusing microfluidic device employing a design, first proposed by Chang et al., composed of two interrogation regions for the fluorescence quantification of cultured cancer cell lines in test samples prepared in the laboratory. The detection of cultured cancer cell lines and, more specifically, the detection of circulating tumor cells (CTC) has been linked to key aspects of early detection, diagnosis, prognosis and monitoring of cancer (Dawson et al. 2013). HER2 (from human epidermal growth factor receptor 2) and EpCAM (from Epithelial cell adhesion molecule) were selected as cell membrane targets to recognize tumor cells of HER2 positive breast cancer (Mitri et al. 2012; Maetzel et al. 2009). The efficiency of the optofluidic platform is demonstrated on samples with different ratios of cancer cell lines with specific antibody expression. This optofluidic system includes a setup designed to perform simultaneous acquisition of the signals at the two interrogation regions of the microfluidic chip. Both pumping and fluorescence light collection at the interrogation regions are carried out employing specific optical fibers according to their rol during the measurement process, allowing a compact, portable, inexpensive and easy to produce design that makes it valuable for point of care applications. Some authors have applied correlation analyses to their obtained data in order to improve their microfluidic device's sensitivity without the need of using additional signal processing filtering devices (Lien et al. 2005, Schonbrun et al. 2011). In our case, we exploit the advantages provided by integrated optical fibers to do independent measurements at each interogation region and perform a correlation analysis without the need of an external apparatus (i.e., a microscope or a laser) which can seriously compromise the portability of the setup and increase the cost. The results are presented in the last part of this work in a cytometer-like graphical representation highlighting the results in the signal analysis after the correlation process. The data series and the results are interpreted in order to improve the confidence on positive events detection.

2 Fabrication of PDMS microfluidic chips

Among all materials used in microfluidic chips fabrication, PDMS is probably the one that offers the best compromise between quality finish and ease of construction. Given the need of incorporating optical fibers and the level of precision required for its correct positioning, we opted for photolithography techniques to produce our microfluidic device. Two main steps were followed in order to construct PDMS chips, SU8 mould fabrication and O_2 plasma bonding prior to optical fiber positioning.

2.1 SU8 mould fabrication

SU8 moulds were fabricated employing standard photolithography techniques widely used in mould construction for PDMS. Photolithography requires a photomask to replicate geometric structures over SU8 negative photoresist. Given the height required for the channels, we opted to use a highly viscous photoresist (SU8-2150, MicroChem Corp.). The photomask used was a 4 inches chromium mask whose microfluidic chip pattern was engraved using a submicron resolution UV lithography laser (DWL 66fs from Heidelberg Instruments). For a single chip elaboration two moulds were required, one containing the structures for the base of the chip, microfluidic channels and grooves for the optical fibers and another one from which the channels for the cover, devoted to vertical sample flow focusing, were casted.

The width for the optical fibers grooves was set during the photomask elaboration at $120\,\mu m$, $5\,\mu m$ below the diameter of the stripped optical fiber to ensure a proper grip between the fiber clading and the PDMS. Care was put during the design of the photomask so that, after the realization of the SU8 master, the channels containing the pumping fibers and the collection fibers would be aligned in such a way that the axis of the fibers would intersected exactly in the middle of the microfluidic channel once they were positioned, at the intersection of the pumping beam of light and the focused sample flow.

The spin-coating process allowed to obtain an SU8 thickness of approximately $120\,\mu m$; the required thickness to obtain channels in the PDMS whose depth will be enough to prevent fibers from protruding too much and to keep them at a constant height with respect the fluidic channel. Standard steps in photolithography are then followed to produce the moulds, namely, soft-bake of the SU8, edge bead removal (EBR), exposition to UV light, post exposure bake (PEB), development of the cross-linked SU8 and Si wafer mould cleaning with O_2 plasma. The SU8 masters were then placed at the bottom of an aluminium foil container and degassed PDMS (Sylgard 184 from Dow Corning) was later poured inside the containers and left to cure at 80°C for 2 hours. After curing, the PDMS slabs were peeled and prepared for plasma bonding.

2.2 PDMS bonding and optical fiber positioning

The PDMS surfaces were irreversibly bonded together exposing the surfaces to a RIE generated oxygen plasma under the following conditions: power: $10\,W$, oxygen flow rate: $50\,sccm$, pressure: $80\,mTorr$ and time: $20\,s$. Figure 1 shows an ESEM image of both interrogation zones with pumping and collecting fibers inserted for illustration purposes. A total of four single-ended FC connectorized optical fiber patch cords were inserted in a single chip. To ensure a proper illumination from the pumping fiber and a clean diverging gaussian beam in the interrogation zone, the fibers were cleaved and later observed in the microscope to verify a clean cut of the face of the fiber before inserting them by hand in the dedicated groove entrances located at both sides of the chip. Likewise, flat and homogeneous fiber cleaves guaranteed an optimal light harvesting for the collection fibers. Each groove end was wetted with a droplet of ethanol which entered inside the groove by capillarity. This reduced the friction and helped during the process of fiber insertion.

3 Experimental setup and employed materials

3.1 Microfluidic chip geometry

Our microfluidic chip consisted essentially of a 3D hydrodynamic focusing chip with two interrogation zones. The distance between each interrogation zone is $1\,mm$ and the width of the microfluidic channel is $100\,\mu m$ while the depth of the channels was set by the

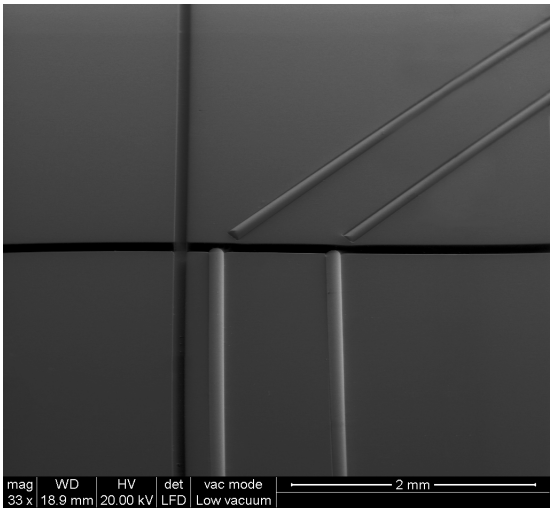

Fig. 1 ESEM image of the lower PDMS slab exposing the t-junction, where lateral focusing takes place, and the two interrogation zones each comprising one pumping fiber, perpendicularly oriented to the fluidic channel, and a collecting fiber oriented at 45°.

diameter of the fibers to be inserted in the microfluidic chip at $125\,\mu m$. As it can be seen in Figure 1 and Figure 2(a), the two input single mode fibers (Custom 460HP optical fiber patch cable from Thorlabs Inc., Newton, NJ, USA) of the microfluidic chip were oriented perpendicularly to the microfluidic channel. Typical pumping powers inside the microfluidic channel during the measurement process were of the order of $10\,mW$ and the mode field diameter of the fiber is around $3.5\,\mu m$. We chose single mode fibers to ensure a small enough beam spot, of the order of the size of the cells, to avoid multiple cell detection at the interrogation zone. Fluorescence collection in each interrogation zone was accomplished by means of two $62.5\,\mu m$ core high numerical aperture ($NA = 0.275$) multimode optical fibers. Each collecting fiber was located at the other side of the microfluidic channel at an orientation of 45° with respect the axis of the pumping fiber. This prevents pumping light from being collected by these fibers allowing pumping light to pass freely through the bulk PDMS without being collected. Such a big core and numerical aperture helps in obtaining an uninterrupted fluorescence signal acquisition from the cells as they move through the length of the pumping region.

Figure 2(b) illustrates the two-level 3D focusing channel design. The sample flow, containing cells, and one of the sheath flows, devoted to vertically focus the sample flow from above, are injected through channels located in the upper level (in the picture, the two right-most vertical channels). These channels are contained within the PDMS cover of the chip making its positioning during the PDMS bonding procedure a critical step. In a second step, the sample flow is further vertically focused from the bottom using another channel located at the lower level (channel running from right to left). Lastly, a conventional lateral focusing is applied to the flow in the lower level of the channel arrangement at the t-junction. The independent treatment of each input flow allowed, not only to adjust the area of the central focused flow stream, but also to position said focused flow within the microfluidic channel with respect to the microchannel walls.

3.2 Setup description

The pumping light for both independent interrogation zones was generated by a single laser diode (06-01 Series from Cobolt) with and integrated FC/PC optical fiber coupler mated to a 1X2 single mode fiber splitter with a splitting ratio of 50 % @473nm (FC488-50B-APC-1 from Thorlabs). The two outputs of the splitter were then mated to each one of the two input single mode fibers of the microfluidic chip.

The two output fluorescence collection multimode patch fibers of the microfluidic chip were directly connected to two photomultiplier tubes (R928 from Hamamatsu), each of them individually enclosed in an aluminium housing (PXT1/M from Thorlabs), using an FC connector. To avoid pumping light from reaching the photomultiplier tubes (pumping light flashes originated mainly from scattered light in the cells) two 500 nm cut-off wavelength longpass filters (FELH0500 from Thorlabs) were located in both aluminium housings between the optical fiber tip and the photocathode. Additional bandpass filters (86-988 and 33-330 from Edmund Optics) were placed in series after each longpass filter to allow the selected wavelength transmission at each photomultiplier detector, red and green light coming from the first and second interrogation zones respectively. Both photomultiplier tubes were

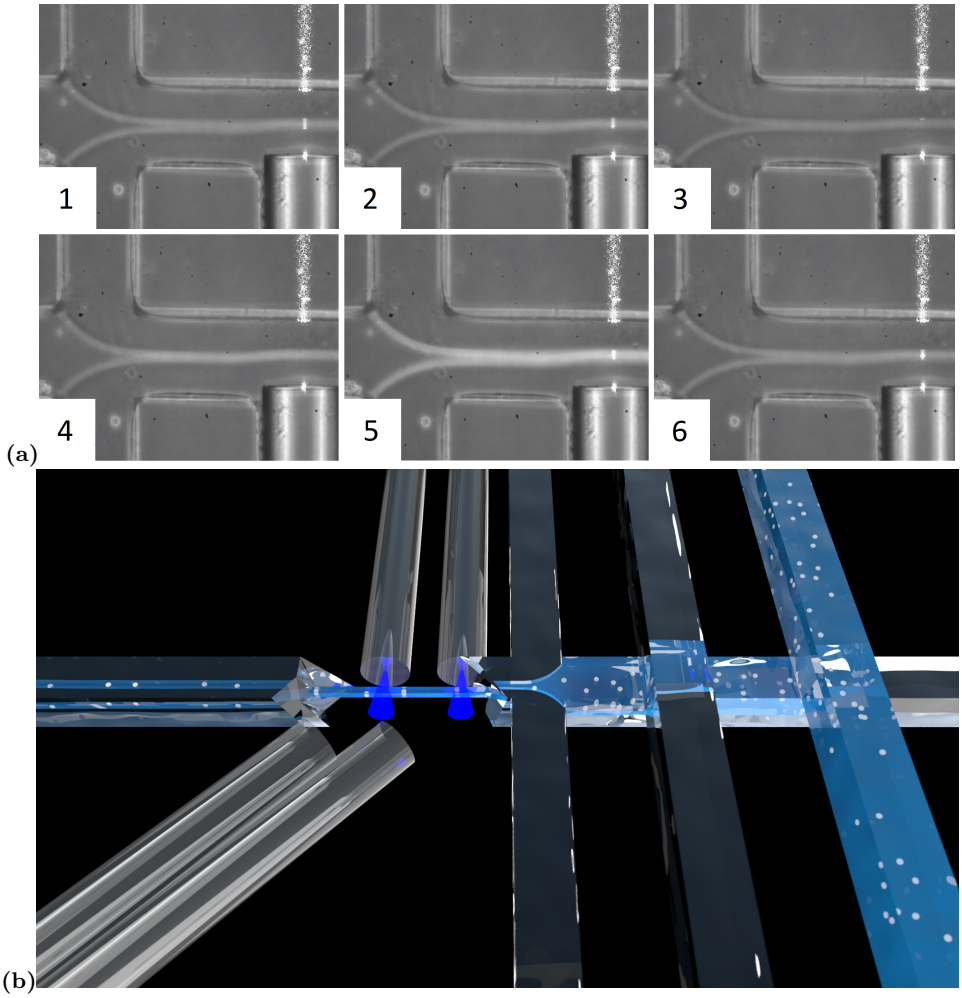

Fig. 2 a) Frame captures of a video demonstrating 3D focusing and exposing the t-junction and the first interrogation zone. The use of a pressure controller allowed for an accurate positioning of the 3D focused sample relative to the pumping light beam; applying a sequentian variation of pressures (1, 2, 5, and 6 slides) a scattered blue light path was visible in the focused sample flow stream only when the stream intersected the pumping beam -the light was probably scattered by the sample's saline solution particles-. (3 and 4) As soon as the height of the focused sample was increased or lowered for a given distance, the light path disappeared and no signal was detected in the detectors. The divergence of the beam is shown as it scatters while propagating through the PDMS. b) 3D render to illustrate the different stages of the hydrodynamic focusing and the optical pumping applied to the cells. To better understand the flow behavior, the sample flow (containing white spheres representing cells) is highlighted in blue and the sheath flows have been removed at both interrogation regions to expose the focused stream.

directly connected through BNC cables to an oscilloscope (TDS 1012B from Tektronix) to simultaneously visualize fluorescence bursts as the cells intersected the pumping volume. A two channel home-made voltage follower with a saturation voltage of 9 V was then connected to the voltage signal from the oscilloscope (employing its internal resistance as the output impedance) and a data acquisition card (NI USB-6212 BNC from National Instruments) was used in order to acquire the signal data from both channels.

The observation of the microfluidic chip under an inverted microscope (IN480TC-FL from AMScope) yield a clear image of the focusing of the sample fluid and ensure a proper alignment with the pumping light as the measurement process was taking place. Control over five independent channels was required in order to

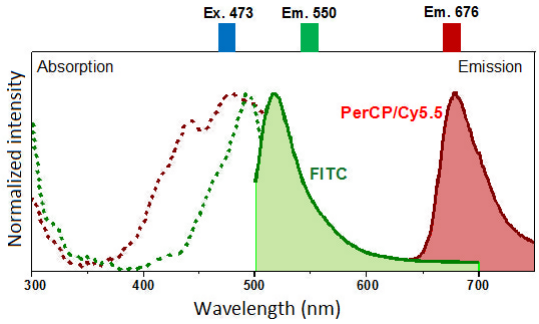

Fig. 3 Spectral absorption (doted lines) and emission curves for FITC and PerCP/Cy5.5.

obtain an adjustable hydrodynamically focused flow of the sample. Two pressure controllers (OB1-mk3 from Elveflow) were employed for that purpose.

3.3 Cell line preparation

To test the performance of the device we selected two cell lines: AU-565 cancer cells derived from mammary breast expressing HER2 and EpCAM receptors and RAMOS, HER2 and EpCAM negative, obtained from the American Tissue Culture Collection (ATCC). The cells were cultured in RPMI media supplemented with 10% fetal bovine serum, at 37° in a 5 % CO_2 atmosphere. Accordingly, to identify the positive cells we employed anti-HER2 and anti-EpCAM antibodies, labeled with fluorescein isothiocyanate (FITC, with green 532 nm emission) and peridinin-chlorophyll-protein cyanin-5.5 (Per-CP/Cy5.5, red 676 nm emission), respectively (from Abcam) as described in Pedrol et al. (2017). These fluorescent reporters were chosen based on their absorption properties in the blue spectral range as seen in Figure 3, which fit perfectly with the laser excitation wavelength (473 nm), and their well-separated emission bands in the visible range. The capability of the optofluidic chip to detect fluorescent-stained cells was tested on samples consisting of AU-565 (+) mixed with RAMOS (-) cells at different ratios (1:1, 1:10, 1:100 and 1:1000).

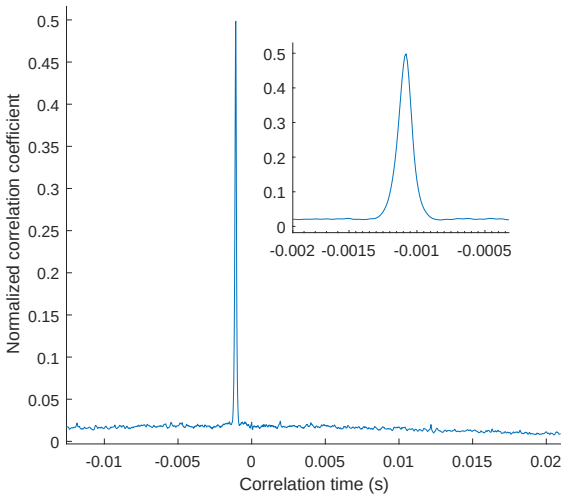

Fig. 4 Cross-correlogram of the green and red fluorescence signals. The inset shows a well defined peak at $\triangle t = -0.00108\,s$.

4 Results and discussion

4.1 Peak pairing algorithm

Raw experimental data was composed of two voltage versus time series detected by both PMT and stored by the data acquisition software. A cell flowing inside the microfluidic chip will eventually cross an interrogation zone and its fluorescence (or autofluorescence) signal will be, ideally, detected by both PMT as the cell passes by both interrogation zones. Such event is represented as a peak at each of the two individually generated files for each of the interrogation zones when plotted.

In the case of the detection of a cell (the simultaneous detection of a signal in the red and green channels), there must exist redundancy in the obtained data assuming that both interrogation zones are exact copies of one another and the fluorescence harvesting process is the same in each pumping volume -the data files for each channel must express some degree of similarity when a correlation analysis is applied-. To automatically consider two given peaks from signals proceeding from different channels as associated to the same cell, the following steps are taken. First, the shift between the red and green channel signals is measured employing a correlation measurement (Fig-

ure 4). The pairing algorithm then performs a primary peak detection in the signals from both channels which yields to a list of their temporal positions as well as their amplitude value. A one-to-one peak association between both channels is then applied by pairing every peak location in the first channel to peaks in the second channel that are temporarily displaced the same distance found in the correlation measurement up to a given error range. This error range is in turn a function of the width of a gaussian fitting of the correlation function; given that the spacing between the interrogation zones is constant, the wider the correlation function, the bigger is the variance in the velocity for the detected cells. We believe that such variance may originate from a small variation in the position of the trajectories of the different measured cells contained within the focused stream as they pass through the interrogation regions, leading to a small difference in their velocity that stems from the parabolic velocity profile inside the microfluidic channel. Once all the paired peaks have been identified, the two fluorescence signal amplitudes (red and green amplitudes), corresponding to a single cell, are collected to be later represented. This analysis method allowed to minimize the errors due to false detections (i.e., two events have to be independently detected at two interrogation regions and correctly correlated to be accounted as a detected cell) improving the reliability with respect conventional microfluidic chips that, although capable of multicolor fluorescence detection, do not take advantage of simultaneous multiple signal acquisition.

We also introduced in the code the ability to discard detected peaks with abnormal shape (i.e., peaks with a too wide waist and/or peaks with a saturated amplitude, mainly peaks that are caused by cell aggregates). The geometry introduced in the fluidic chip -mainly the pumping fiber in direct contact with the fluidic channel- allowed to obtain a very well defined gaussian pumping profile over the sample stream flow of around $7-8\,\mu m$ in waist. This ensures that any unexpected widening in a detected peak in the $V\,(t)$ plot can only come from a dramatic change in the size of the detected body being measured. An eventual widening of the pumping beam waist wouldn't allow to apply this discarding method forcing to have to rely more on the uncertainty of rejecting peaks by their abnormally big amplitude instead, ignoring if such peaks

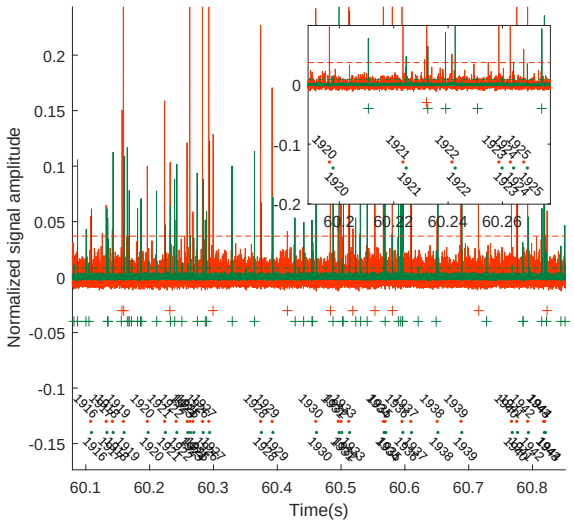

Fig. 5 Voltage versus time plots for red and green channels and the results after the pairing process in the 1:1 ratio sample. The code identifies and labels the paired peaks at each channel tagging their temporal position with a solid dot with matching color corresponding to the channel of origin. Unpaired peaks -peaks only detected in one of the channels or without a corresponding peak at the stablished shift- are also marked with red or green colored crosses. Detection thresholds for each channel are also represented. Notice the consistent slight displacement in the paired peaks positions in the green channel with respect their corresponding paired peak in the red channel due to the time delay in the measurement of a given cell between the first and the second interrogation zones.

are caused by a big cell (or aggregate of cells) or by a small cell with heavy staining. If not corrected, such events may produce an important bias when dealing with patient's real blood sample for which very small ratios are expected for CTCs. Figure 5 illustrates the final result of the pairing process.

4.2 Data analysis

For each analyzed sample, we recorded the fluorescence signals both in the red and green channels for $100\,s$ at a sample rate of $10^5\,S/s$. Each peak in the voltage versus time plots represents the detection of a cell passing through each detection zone. We could observe that the mean peaks' intensities in the green channel are significantly higher than that in the red

channel, indicating the higher efficiency of FITC (and/or autofluorescence intensity in that part of the spectrum) compared with PerCP. In any case, FITC fluorescence signal strength was not intense enough to allow for a cell classification in terms of a detection threshold like in the case of PerCP.

Due to the presence of the HER2 and EpCAM receptors in the AU-565 line, these cells were marked with both PerCP and FITC, so they will both emit red and green fluorescence. RAMOS cells (not marked) will emit only due to autofluorescence mechanisms. Under 473 nm pumping, the autofluorescence of the cell in the green part of the spectrum is similar to that of cells marked with FITC. Red autofluorescence, on the other hand, is much less intense than the fluorescence emission of PerCP stained cells. This fact explains the fact that, in all performed measurements, there is a larger number of detected green peaks (mainly because of the strong green non-specific autofluorescence component in both cell lines with a small contribution from FITC fluorescence), than peaks in the red channel (corresponding to AU-565 cells marked with PerCP and weak autofluorescence in the red from both cell lines).

The signal in the downstream detection area is delayed respect to the other, but both signals show a good correlation due to the laminar behavior of the flow, that imposes that each particle that passes through the first area, will likely cross the second section in the same conditions after a time delay $\triangle t = D/u$, where D is the separation between detection zones ($1\,mm$) and u is the velocity of the cell.

Figure 4 shows a segment of the cross-correlogram showing a well-defined peak at $\triangle t = -0.00108\,s$, indicating that the mean velocity of the cells is $u = 926\,mm/s$. Cross-correlation gives a quite precise measurement (error <1%) of the velocity of the flow and allows to accurately compare the passing of the particles in both zones. The simultaneous analysis of both signals reduces the effect of the noise in the signals and gives a robust method for counting cells in very noisy situations.

Fluorescence intensity data for paired peaks is represented as scatter plots. Each dot in the graph represents a detected cell and their coordinates are the fluorescence signal amplitudes measured as the prominences of the detected peaks. In order to set a threshold for the positive events we measured two samples, one containing exclusively AU-565 cells with specific PerCP and FITC labeling, which would represent positive detections, and another one containing RAMOS cells, whose detection would correspond mainly to negative events. When representing this results a bimodal distribution appears with one of the modes, corresponding to AU-565 cells that express HER2 labeled PerCP, having a higher red signal. The other mode, with lower red signal, is produced by the weak red autofluorescence of the unlabeled RAMOS cell line corresponding to negative population. A standard $k-means$ clustering method is then applied to each individual data series setting a random initial centroid for each population. Once the classification method has converged, it produces a new centroid and the detection threshold for the red channel is set in between the new generated centroids for positive and negative events (Figure 6).

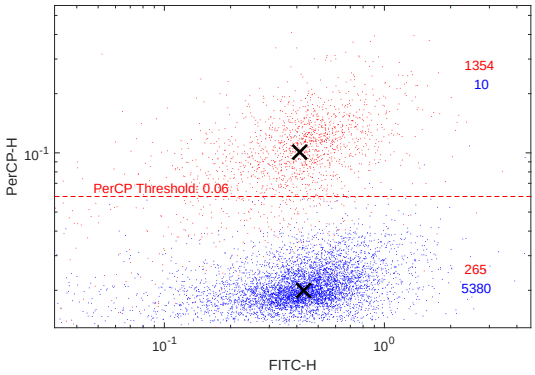

Fig. 6 Scatter plot of fluorescence signal amplitudes for AU-565 cells (red scatter cloud) and a sample containing RAMOS cells (blue cloud). A $k-means$ analysis is applied over the clusters and the obtained classes' centroids (black crosses) coordinates are $C_{AU-565} = (0.4, 0.1)$ and $C_{RAMOS} = (0.43, 0.02)$. The detection threshold is located between the centroids in the $y-$direction (red fluorescence scale) at an equidistant position to both centroids, at 0.06. The numbers at the upper and lower halves, the positive and negative region respectively, represent the counted events in said regions for AU-565 cells (red) and RAMOS cells (blue).

After setting the threshold in the red channel, a series of measurements were taken over some samples containing different ratios of cell lines prepared in the laboratory (Figure 7; AU-565:RAMOS; 1:1, 1:10, 1:100

and 1:1000) and the results were compared with the theoretical expected known value. We also apply a $k-means$ classification method in this step employing the centroids' coordinates we found in the previous step as an initial guess. The code also counts the number of events at both, the negative and the positive regions, from which the deduced ratios will be later calculated.

Table 1 summarizes the results of the classification of the analyzed samples. It includes the center of the negative and positive classes (in linear-scale coordinates), the number of cells detected in each class and the ratio between the number of cells detected by the pairing algorithm. The ratios obtained matches well with the expected ones for the samples with higher concentration of AU-565 cells. For the 1:1 and 1:10 samples, the matching is almost perfect, but the quality of the matching reduces as the concentration of AU-565 cells diminishes. For example, in the 1:100 sample the result is three times greater than expected, and in the 1:1000 sample, this factor increases to just above 5.

5 Conclusions

The laboratory-engineered samples served as a reliability test to detect two kind of cell populations in terms of their fluorescence footprint. It was also useful to ensure that our system may enable a fast detection method of CTCs in a real blood sample without the need of any dramatic modification in the original design. Although acquisition time was not a determining factor during our experiment, we managed to detect just over 30.000 cells in a single $100\,s$ run from samples with cell concentrations of the order of $10^6\,C/ml$. Given that this cell concentration and the employed flow rates can be further increased, it is reasonable to think that CTC tests can also be performed in this device. In that aspect, the major challenge is to be able to analyse a big number of cells to obtain a statistically representative number of events ($10^6 - 10^7$), an aim beyond our "proof of concept" aproach. In addition of improving the reliability of cell detection by means of correlation measurements, our system allowed to easily discard cell aggregates detection events (in most of the data we treated) thanks to an individual peak geometry analysis. The conjunction of 3D hydrodynamic focusing and the features provided by optical fibers, i.e., a small pumping volume from the single mode fiber and the efficient fluorescence light harvesting in the high NA fibers, turned out to produce satisfactory results. We believe that all these features can be easily incorporated to almost any microfluidic device providing major improvements in the field of microfluidics devoted to cytometric analysis. Furthermore, this sensing platform can be easily extended to the investigation of other tumors by employing different selective antibodies.

Acknowledgements This project is supported by Spanish government and MAT2016- 75716-C2-1-R (AEI/FEDER, UE), Ministerio de Economia y Competitividad (MAT2013-47395-C4-4-R, TEC2014-55948-R and CTQ2014-59808R), Generalitat de Catalunya (2014SGR1358 and2014SGR480) and HM Group Hospitales..

References

1. Bouzigues C, Gacoin T, Alexandrou A (2011) Biological applications of rare-earth based nanoparticles. ACS Nano 5(11) 8488–8505
2. Català C, Mir-Simón B, Feng X, Cardozo C, Pazos-Pérez N, Pazos E, de Pedro SG, Guerrini L, Soriano A, Vila J, Marco F, Garcia-Rico E, Álvarez-Puebla R (2016) Online SERS quantification of staphylococcus aureus and the application to diagnostics in human fluids. Adv Mat 1(8)
3. Chang-Yeng DA, Eich RK, Gale BK (2005) A monolithic PDMS waveguide system fabricated using soft-lithography techniques. J Lightw Technol 23(6) 2088-2093
4. Chen HT, Wang YN (2009) Optical microflow cytometer for particle counting, sizing and fluorescence detection. Microfluid Nanofluid 6(4) 529–537
5. Daniele MA, Boyd DA, Mott DR, Ligler FS (2015) 3D hydrodynamic focusing microfluidics for emerging sensing technologies. Biosens Bioelectron 67 25–34
6. Dawson SJ, Tsui DWY, Murtaza M, Biggs H, Rueda OM, Chin SF, Dunning MJ, Gale D, Forshew T, Mahler-Araujo B, Rajan S, Humphray S, Becq J, Halsall D, Wallis M, Bentley D, Caldas C, Rosenfeld N (2013) Analysis of circulating tumor DNA to monitor metastatic breast cancer. N Engl J Med 368, 1199-1209
7. Edel JB, de Mello AJ (2003) Determination of single particle flow velocities in microchannels using a maximum likelihood estimator method. Phys Chem Chem Phys 5(18) 3973–3978
8. Garcia D, Ghansah I, LeBlanc J, Butte MJ (2012) Counting cells with a low-cost integrated microfluidics-waveguide sensor. Biomicrofluidics 6(1) 014115

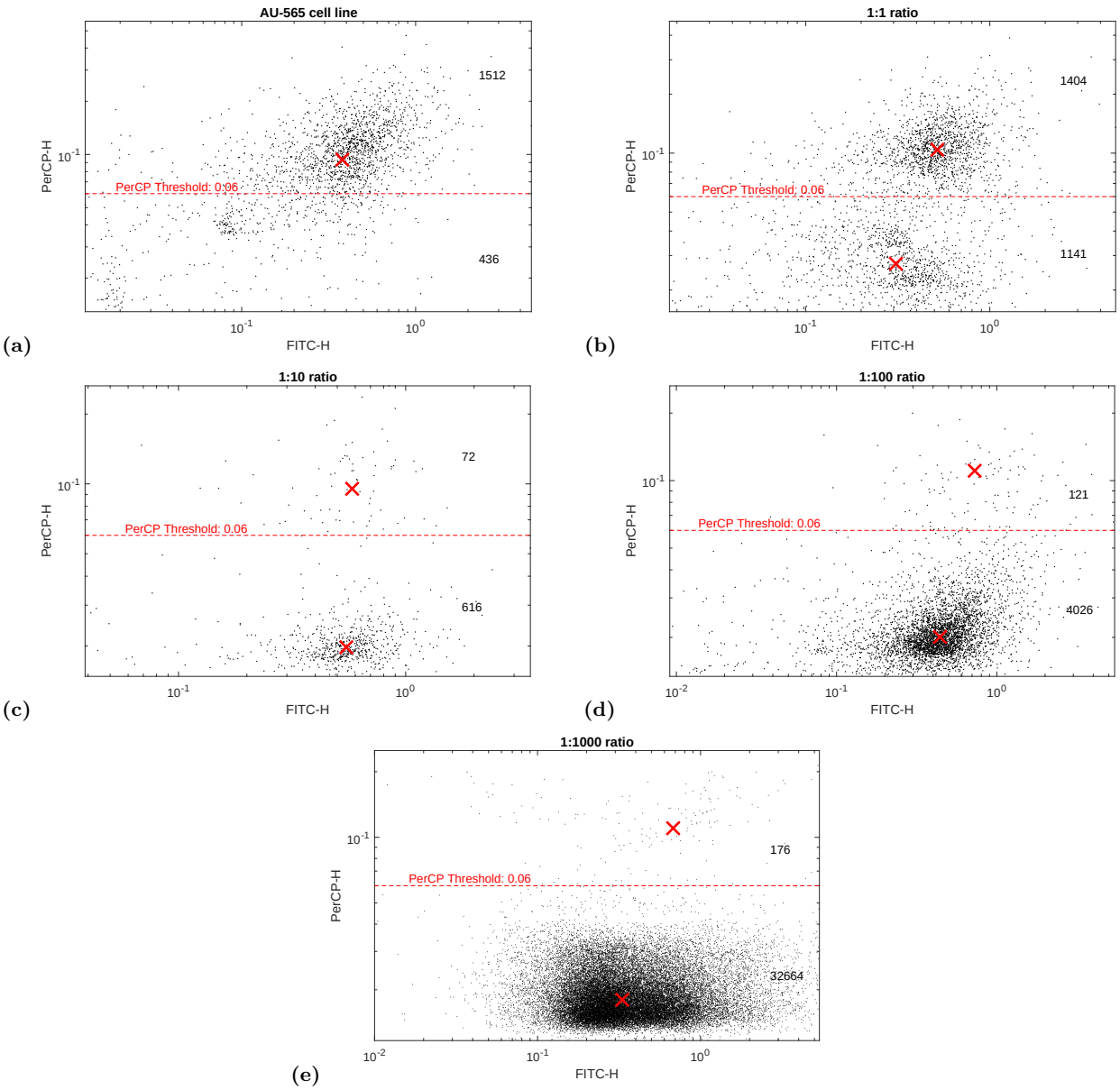

Fig. 7 Scatter plots for samples with different ratios of cell lines (AU-565:RAMOS) in terms of their red and green fluorescence signal. Clusters' centroids position after the application of a $k-means$ method are marked with red crosses. As expected, when the ratio decreases (increased content of RAMOS cells), the lower region becomes more populated. In order to obtain a reliable measurement for the 1:100 and the 1:1000 ratios, the concentration in those samples was increased, so that the number of detected events could be taken as representative of such low concentrations. There is a tendency for the centroids position in the upper halves (positive detection) to be slightly displaced towards higher green fluorescence values. This is probably due to a small contribution of the FITC emission on the overall signal.

Sample (AU-565:RAMOS)	Positive centroid	Negative centroid	Positive counts	Negative counts	Ratio
AU-565 only	(0.38, 0.094)	x	1512	436	x
1:1	(0.52, 0.104)	(0.31, 0.027)	1404	1141	1:0.81
1:10	(0.58, 0.095)	(0.55, 0.019)	72	616	1:8.56
1:100	(0.73, 0.111)	(0.44, 0.020)	121	4026	1:33.27
1:1000	(0.68, 0.11)	(0.33, 0.018)	176	32664	1:185.59

Table 1 Results obtained by the optofluidic device after the measurement of samples with different cell line concentration.

9. Gervais L, de Rooij N, Delamarche E (2011) Microfluidic chips for point-of-care immunodiagnostics. Adv Mater 23(24) H151–H176
10. Jiang L, Wang W, Chau Y, Yao S (2013) Controllable formation of aromatic nanoparticles in a three-dimensional hydrodynamic flow focusing microfluidic device. RSC Adv 3(39) 17762-17769
11. Knight JB, Vishwanath A, Brody JP, Austin RH (1998) Hydrodynamic focusing on a silicon chip: mixing nanoliters in microseconds. Phys Rev Lett 80(17) 3863–3866
12. Konokhova AI, Yurkin MA, Moskalensky AE, Chernyshev AV, Tsvetovskaya GA, Chikova ED, Maltsev VP (2012) Light-scattering flow cytometry for identification and characterization of blood microparticles. J Biomed Opt 17(5), 057006
13. Lien V, Zhao K, Berdichevsky Y, Lo YH (2005) High-sensitivity cytometric detection using fluidic-photonic integrated circuits with array waveguides. IEEE J Sel Top Quantum Electron 11(4) 827-834
14. Lu M, Ozcelik A, Grigsby CL, Zhao Y, Guo F, Leong KW, Huang TJ (2016) Microfluidic hydrodynamic focusing for synthesis of nanomaterials. Nano Today 11(6) 778-792
15. Maetzel D, Denzel S, Mack B, Canis M, Went P, Benk M, Kieu C, Papior P, Baeuerle PA, Munz M, Gires O (2009) Nuclear signalling by tumour-associated antigen EpCAM. Nat Cell Biol 11(2) 162–71
16. Mao X, Nawaz AA, Lin SCS, Lapsley MI, Zhao Y, McCoy JP, Huang TJ (2012) An integrated, multiparametric flow cytometry chip using 'microfluidic drifting' based three-dimensional hydrodynamic focusing. Biomicrofluidics 6(2), 024113
17. McDonald JC, Whitesides GM (2002) Poly(dimethylsiloxane) as a material for fabricating microfluidic devices. Acc Chem Res 35(7) 491-499
18. Mitri Z, Constantine T, O'Regan R (2012) The HER2 receptor in breast cancer: pathophysiology, clinical use, and new advances in therapy. Chemother Res Pract 2012 743193
19. Pazos-Pérez N, Pazos E, Català C, Mir-Simón B, de Pedro SG, Segalés J, Villanueva C, Vila J, Soriano A, de Abajo FJG, Álvarez-Puebla R (2016) Ultrasensitive multiplex optical quantification of bacteria in large samples of biofluids. Sci Rep 6, 29014
20. Pedrol E, Garcia-Algar M, Massons J, Nazarenus M, Guerrini L, Martínez J, Rodenas A, Fernandez A, Aguiló M, Estevez LG, Calvo I, Olano A, Garcia-Rico E, Díaz F, A. Alvarez-Puebla R (2017) Cytometer-like optofluidic device for the quantification of circulating tumor cells in breast cancer. Submitted to Sci Rep
21. Pelaz B, Alexiou C, Álvarez-Puebla R, Parak WJ (2017) Diverse applications of nanomedicine. ACS Nano
22. Schaap A, Rohrlack T, Bellouard Y (2012) Optical classification of algae species with a glass lab-on-a-chip. Lab Chip 12(8) 1527–1532
23. Schafer D, Gibson EA, Salim EA, Palmer AE, Jimenez R, Squier R (2009) Microfluidic cell counter with embedded optical fibers fabricated by femtosecond laser ablation and anodic bonding. Opt Express 17(8) 6068–6073
24. Schonbrun E, Steinvurzel PE, Crozier KB (2011) A microfluidic fluorescence measurement system using an astigmatic diffractive microlens array. Opt Express 19(2) 1385-94
25. Testa G, Persichetti G, Bernini R (2015) Micro flow cytometer with self-aligned 3D hydrodynamic focusing. Biomed Opt Express 6(1) 54–62
26. Tung YC, Zhang M, Lin CT, Kurabayashi K, Skerlos SJ (2004) PDMS-based opto-fluidic micro flow cytometer with two-color, multi-angle fluorescence detection capability using PIN photodiodes. Sens Actuators B 98 356–367
27. Wang M, Mi C, Zhang Y, Liu J, Li F, Mao C, Xu S (2009) NIR-responsive silica-coated NaYbF4:Er/Tm/Ho upconversion fluorescent nanoparticles with tunable emission colors and their applications in immunolabeling and fluorescent imaging of cancer cells. J Phys Chem C, 113(44) 19021–19027
28. Weigl BH, Bardell R, Schulte T, Battrell F, Hayeng J (2001) Design and rapid prototyping of thin-film laminate-based microfluidic devices. Biomed Microdevices 3(4) 267–274